2026 International Conference on Unmanned Aircraft Systems (ICUAS)
June 15-18, 2026. Corfu, Greece

Full Actuator Nonlinear Dynamic Inversion for Enhanced Hybrid UAV Control

Justin P. G. Dubois*, Evangelos Ntouros†, Ewoud J. J. Smeur‡

***Abstract*— Expanding the operational capabilities of Micro Air Vehicles (MAVs) hinges on control systems that manage highly nonlinear dynamics across broad flight envelopes. Incremental Nonlinear Dynamic Inversion (INDI) is popular for its simplicity and modest modeling needs, but its assumption of infinitely fast actuators and neglect of state-dependent effects limit performance when actuators have slow or heterogeneous dynamics or when aerodynamic effects are significant. Actuator Nonlinear Dynamic Inversion (ANDI) overcomes these limitations by explicitly incorporating state-dependent dynamics and finite actuator bandwidth into the control law, enabling improved tracking performance across diverse actuator configurations.**

This work implements the full ANDI stabilization controller on the *Cyclone*, a hybrid MAV tail-sitter, using cascaded complementary filtering for state estimation. Simulation and flight experiments validate the approach and assess whether this compensation yields practical performance gains, establishing ANDI as a viable, generic control solution for MAVs. Code is available at `https://github.com/tudelft/paparazzi/tree/feat_stabilization_andi_controller`

***Index Terms*— actuator nonlinear dynamic inversion, feedback linearization, hybrid UAV, incremental nonlinear dynamic inversion, nonlinear control, tail-sitter**

I. Introduction

MAVs are experiencing rapid growth and adoption in an increasingly wide range of industrial applications where they address the need for agile, cost-effective, and versatile aerial platforms. To satisfy the mission requirements, these vehicles are often tailored to best fulfill a specific mission, resulting in a diverse landscape of vehicle types, including fixed-wing, rotary-wing, and hybrid configurations [1]. Hybrid Unmanned Aerial Vehicles (UAVs), such as tail-sitters and tiltrotors, combine the vertical takeoff and landing capabilities of rotary-wing aircraft with the efficient forward flight characteristics of fixed-wing designs, enabling a broader range of operational scenarios

This diversity in airframe design poses challenges for flight control development and deployment. Their low cost and small size drive tight budgets and rapid prototyping, increasing demand for generic, adaptable controllers deployable across platforms. However, unconventional airframes can exhibit highly nonlinear and coupled dynamics, making reliable high-performance control challenging [1]. Linear controllers relying on local linearization often struggle across wide operating envelopes. Therefore, nonlinear approaches are needed that remain easy to implement and transferable across MAV configurations.

INDI has emerged as a promising control technique to address these challenges. INDI leverages sensor feedback to locally linearize the dynamics of the vehicle, effectively transforming the system into an equivalent linear one over a broad operating envelope without needing a full model of the system dynamics [2]. This enables the use of classical linear control techniques for systems with significant nonlinearities. Furthermore, INDI decouples airframe-dependent characteristics from the controller design, thus facilitating the reuse of control architectures across different UAV platforms. INDI has demonstrated excellent performance on a variety of MAVs [3–5].

INDI limitations in modeling actuator dynamics and state-dependent terms motivate advanced techniques that address these effects more directly in the feedforward path.

To overcome these limitations, Steffensen et al. [6] developed ANDI, which explicitly models both state-dependent drift dynamics and finite actuator dynamics directly in the feedforward path of the control law. By compensating for these effects in the feedforward path, rather than relying on feedback correction, ANDI enables faster error rejection and improved tracking performance. ANDI has been validated in simulation and shown to offer theoretical advantages such as well-defined error dynamics and exact reference tracking [6]. Previous experimental work by De Ponti et al. [7] has demonstrated ANDI's effectiveness in compensating for actuators with differing bandwidth. However, the ability to compensate state-dependent effects through the feedforward path has yet to be experimentally validated on a real MAV platform.

This project aims to bridge this gap by implementing and experimentally validating full ANDI with explicit state-dependent compensation on a tail-sitter MAV. The *Cyclone* tail-sitter exhibits strong state-dependent effects, including lift and drag caused by the large wing, providing a representative testbed for evaluating feedforward state-dependent compensation. The work comprises: (i) designing and implementing a full ANDI stabilization (attitude) controller with explicit state-dependent compensation; (ii) generating undelayed feedback estimates through a cascaded complementary filter as proposed by Steffensen et al. [8]; and (iii) conducting flight tests to experimentally validate the compensation of state-dependent effects and compare performance against

*Ir. Justin P. G. Dubois is with the Faculty of Aerospace Engineering, Control & Simulation, Delft University of Technology, 2629 HS Delft, The Netherlands (e-mail: jpgdubois@outlook.com). Corresponding author. †Evangelos Ntouros is with the Faculty of Aerospace Engineering, Control & Simulation, Delft University of Technology, 2629 HS Delft, The Netherlands (e-mail: e.ntouros@tudelft.nl). ‡Dr. Ir. Ewoud J. J. Smeur is with the Faculty of Aerospace Engineering, Control & Simulation, Delft University of Technology, 2629 HS Delft, The Netherlands (e-mail: e.j.j.smeur@tudelft.nl).

2026 International Conference on Unmanned Aircraft Systems (ICUAS) | 979-8-3315-9316-2/26/$31.00 ©2026 IEEE | DOI: 10.1109/ICUAS69441.2026.11598601

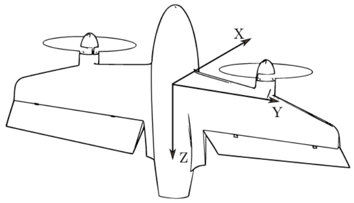

Fig. 1: Diagram of the *Cyclone* tail-sitter UAV with its body axis convention. [9]

the INDI baseline, extending beyond prior actuator-only studies [7].

II. Experimental Platform and Configuration

A. Platform Overview

The experimental platform is the *Cyclone* tail-sitter UAV, a hybrid Vertical Takeoff and Landing (VTOL) platform combining rotary-wing hover capabilities with efficient fixed-wing forward flight [9]. The vehicle transitions continuously across all pitch angles from vertical hover to horizontal forward flight, requiring a globally valid control law. The body frame uses x-axis forward, y-axis right, and z-axis downward (to tail), shown in fig. 1.

B. Actuators and Sensors

Actuation comprises two counter-rotating tractor motors (providing thrust and differential roll control) and elevons (providing pitch and yaw control via symmetric and differential deflections). Both surfaces remain effective in hover due to the propeller slipstream. The vehicle carries an Inertial Measurement Unit (IMU) measuring angular rates and specific forces, with an onboard flight computer running `Paparazzi Autopilot` [10] for sensor acquisition, state estimation, and control execution. Actuator feedback is provided as motor speed and elevon angle measurements.

C. Specific Thrust Modelling

The total specific thrust τ generated by the two propellers is approximated as a linear function of the squared motor rotational speeds, $\omega_{m_l}^2$ and $\omega_{m_r}^2$ for the left and right motors, respectively. The resulting model is expressed in eq. (1).

$$f_\tau(\mathbf{u}) = \tau = c_\tau(\omega_{m_l}^2 + \omega_{m_r}^2) \tag{1}$$

This simple representation is valid for hover and low-speed flight, where inflow angle and induced-velocity coupling are small.

D. Φ-Theory Aerodynamic Model

The aerodynamic model follows the Φ-theory formulation for tail-sitter aircraft, which expresses forces and moments in body-axis velocity components, avoiding singularities inherent to angle-of-attack parameterizations [11, 12]. The exact model structure and parameters are relegated to Dubois [13], to comply with page limits.

III. ANDI Controller Design

ANDI extends INDI by controlling one derivative order higher, enabling explicit compensation for first-order actuator dynamics and state-dependent effects [6]. This section derives the ANDI stabilization law for the *Cyclone* platform and presents the reference model and error controller that shape the closed-loop dynamics.

A. Control Law Derivation

The ANDI attitude control law for the *Cyclone* platform is derived following Steffensen et al. [6], beginning with the state, input, and output vectors in eqs. (2) to (4) respectively.

$$\mathbf{x} = \begin{bmatrix}\omega_x & \omega_y & \omega_z & v_x & v_y & v_z\end{bmatrix}^\top \tag{2}$$

$$\mathbf{u} = \begin{bmatrix}\delta_{e_l} & \delta_{e_r} & \omega_{m_l}^2 & \omega_{m_r}^2\end{bmatrix}^\top \tag{3}$$

$$\mathbf{z} = \begin{bmatrix}\dot\omega_x & \dot\omega_y & \dot\omega_z & \tau\end{bmatrix}^\top \tag{4}$$

The state vector $\mathbf{x}$ contains the body-frame angular rates $\boldsymbol{\omega}$ and linear velocities $\mathbf{v}$, the output vector $\mathbf{z}$ contains the body-frame angular accelerations $\dot{\boldsymbol{\omega}}$ and specific thrust τ, and the control input vector $\mathbf{u}$ contains the left and right servo deflections $\delta_{e_l}, \delta_{e_r}$ and the squared motor rotational speeds $\omega_{m_l}^2, \omega_{m_r}^2$. Squared motor rotational speed is chosen as the control input to linearize the command-to-thrust relationship, exploiting the quadratic relationship between propeller thrust and rotational speed.

Unlike classical INDI, ANDI models actuator dynamics as first-order systems. Motor and elevon bandwidths ($35\,\mathrm{rad\,s^{-1}}$ and $20\,\mathrm{rad\,s^{-1}}$) are collected in $\boldsymbol{\varepsilon}_u$ in eq. (5).

$$\dot{\mathbf{u}} = \boldsymbol{\varepsilon}_u(\mathbf{u}_c - \mathbf{u}), \quad \boldsymbol{\varepsilon}_u = \mathrm{diag}(\varepsilon_{e_l}, \varepsilon_{e_r}, \varepsilon_{m_l^2}, \varepsilon_{m_r^2}) \tag{5}$$

The controlled outputs are angular acceleration and specific thrust, defined in eq. (6).

$$\mathbf{z} = \begin{bmatrix}\dot{\boldsymbol{\omega}} \\ \tau\end{bmatrix} = \begin{bmatrix}\mathbf{f}_m(\mathbf{x},\mathbf{u}) \\ f_\tau(\mathbf{x},\mathbf{u})\end{bmatrix} \tag{6}$$

In Equation (6), both $\mathbf{f}_m(\mathbf{x},\mathbf{u})$ and $f_\tau(\mathbf{u})$ are derived from the aerodynamic and thrust models. The reactive torque from the motors, and the moment generated by elevon angular velocity are neglected in this formulation. Although compensation terms proportional to motor angular accelerations and elevon angular rates can be included [14], these contributions are small compared to the dominant aerodynamic and thrust moments and are further minimized by the slow actuator dynamics.

Differentiating eq. (6) yields the output dynamics in terms of $\dot{\mathbf{x}}$ and $\dot{\mathbf{u}}$, with state-dependent contribution F_x and control effectiveness F_u. The Jacobians are computed symbolically (`MATLAB Symbolic Toolbox`).

$$\dot{\mathbf{z}} = \begin{bmatrix}\ddot{\boldsymbol{\omega}} \\ \dot\tau\end{bmatrix} = \underbrace{\begin{bmatrix}\frac{\partial}{\partial\mathbf{x}}\mathbf{f}_m(\mathbf{x},\mathbf{u}) \\ \frac{\partial}{\partial\mathbf{x}}f_\tau(\mathbf{x},\mathbf{u})\end{bmatrix}}_{F_x}\dot{\mathbf{x}} + \underbrace{\begin{bmatrix}\frac{\partial}{\partial\mathbf{u}}\mathbf{f}_m(\mathbf{x},\mathbf{u}) \\ \frac{\partial}{\partial\mathbf{u}}f_\tau(\mathbf{x},\mathbf{u})\end{bmatrix}}_{F_u}\dot{\mathbf{u}} \tag{7}$$

The term F_x represents the sensitivity of the dynamics to state changes. In prior work by De Ponti et al. [7], this term is neglected under the assumption that the contribution of the state-dependent dynamics $F_x\dot{\mathbf{x}}$ is significantly smaller than $F_u\dot{\mathbf{u}}$. This work retains $F_x\dot{\mathbf{x}}$ to evaluate its impact on tracking performance when state-dependent effects are significant.

The magnitude of the state-dependent term $F_x\dot{\mathbf{x}}$ scales with the rate of state change. For the attitude control problem, this becomes significant during aggressive maneuvers where angular accelerations are large, as the aerodynamic forces and moments that comprise F_x scale with both angular velocity and angular acceleration. Conversely, in quasi-steady-state flight with small angular rates, the state-dependent contribution becomes negligible.

The linearizing control law is obtained by solving eq. (7) for the commanded actuator rate $\dot{\mathbf{u}}_c$, assuming F_u has full row rank in the operational region, admitting a right pseudo-inverse. Introducing the pseudo-control vector $\boldsymbol{\nu} = [\ddot{\boldsymbol{\omega}}^\top \; \dot{\tau}]^\top$ yields the control law in eq. (8).

$$\dot{\mathbf{u}}_c = F_u^\dagger \left(\boldsymbol{\nu} - F_x\dot{\mathbf{x}}\right) \tag{8}$$

Substituting the actuator dynamics eq. (5) and solving for $\mathbf{u}_c$ yields the incremental law in eqs. (9) and (10).

$$\mathbf{u}_c = \boldsymbol{\varepsilon}_u^{-1}\dot{\mathbf{u}}_c + \mathbf{u} \tag{9}$$

$$\mathbf{u}_c = \boldsymbol{\varepsilon}_u^{-1} F_u^\dagger \left(\boldsymbol{\nu} - F_x\dot{\mathbf{x}}\right) + \mathbf{u} \tag{10}$$

The commanded input $\mathbf{u}_c$ adds an increment to the current actuator state $\mathbf{u}$: $\boldsymbol{\varepsilon}_u^{-1}F_u^\dagger\boldsymbol{\nu}$ tracks reference jerk/thrust-rate and $-\boldsymbol{\varepsilon}_u^{-1}F_u^\dagger F_x\dot{\mathbf{x}}$ compensates state-dependent dynamics. Including $\boldsymbol{\varepsilon}_u$ accounts for heterogeneous actuator bandwidths. The bandwidth matrix $\boldsymbol{\varepsilon}_u$ within the pseudo-inverse accounts for heterogeneous actuator dynamics.

B. WLS Control Allocation

To maintain predictable behavior under saturation, Weighted Least Squares (WLS) control allocation prioritizes objectives while respecting actuator limits. Rather than computing the pseudo-inverse directly, the WLS control allocator solves a constrained optimization problem n that minimizes the weighted error while respecting actuator limits in eqs. (11) to (13).

$$\underset{\dot{\mathbf{u}}_c}{\text{minimize}} \left\|\mathbf{W}\left(\boldsymbol{\nu} - F_x\dot{\mathbf{x}} - F_u\dot{\mathbf{u}}_c\right)\right\|^2 \tag{11}$$

subject to the constraints:

$$\dot{\mathbf{u}}_{\text{min}} \leq \dot{\mathbf{u}}_{c,n} \leq \dot{\mathbf{u}}_{\text{max}} \tag{12}$$

$$\boldsymbol{\varepsilon}_u(\mathbf{u}_{\text{min}} - \mathbf{u}_n) \leq \dot{\mathbf{u}}_{c,n} \leq \boldsymbol{\varepsilon}_u(\mathbf{u}_{\text{max}} - \mathbf{u}_n) \tag{13}$$

where $\mathbf{W} = \text{diag}([1000, 100, 1, 10])$ prioritizes x-axis rotation, then y-axis, thrust, and z-axis rotation. The constraints eqs. (12) and (13) enforce rate and position limits.

C. Error Controller Design

The error controller is designed through pole-placement to achieve desired disturbance rejection dynamics in the presence of model-plant mismatches and external disturbances. Conventional linear system theory is used to design and the error controller, leveraging the fact that ANDI linearizes and decouples the system dynamics from the pseudo-control input $\boldsymbol{\nu}$ to the output $\mathbf{z}$.

Considering an additive disturbance D acting on the system at the angular acceleration and specific thrust z, as illustrated in fig. 2. This disturbance represents external forces acting on the MAV and any errors in the inversion due to model mismatch. By assuming the disturbance is independent of the state and input [15], the designed poles remain unaffected by complementary filtering. Consequently, the error controller gains can be designed without explicitly accounting for filtering, with the impact of complementary filtering analyzed subsequently in section III-E.

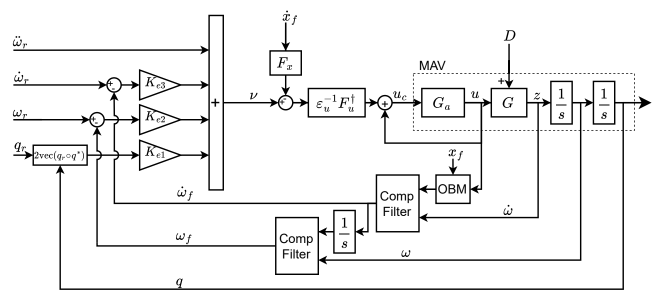

Fig. 2: ANDI attitude control of system G with actuators G_a. The error controller generates pseudo-control input $\boldsymbol{\nu}$ from attitude errors and reference commands. The incremental control law inverts system dynamics while compensating state-dependent effects $F_x\dot{\mathbf{x}}$ to compute actuator commands. Cascaded complementary filters fuse noisy measurements with model-based estimates to provide undelayed feedback of angular acceleration and rates; translational filtering is omitted for clarity.

The pseudo-command vector $\boldsymbol{\nu}$, containing the angular jerk and specific thrust rate, is regulated by a linear error controller designed to track the reference commands and reject disturbances with desired dynamics, as given in eq. (14). A third-order parallel error controller is used for the angular jerk and first-order parallel error controller is used for the specific thrust rate, this allows for attitude and specific thrust reference tracking.

$$\boldsymbol{\nu} = \begin{bmatrix} \ddot{\boldsymbol{\omega}}_r + (\dot{\boldsymbol{\omega}}_r - \dot{\boldsymbol{\omega}})K_{e_3} + (\boldsymbol{\omega}_r - \boldsymbol{\omega})K_{e_2} + 2\,\text{vec}(\mathbf{q}_r \circ \mathbf{q}^*)K_{e_1} \\ \dot{\tau}_r + (\tau_r - \tau)k_{e_\tau} \end{bmatrix} \tag{14}$$

The complete decoupled linearized system including the disturbances and error controller in the Laplace Domain is shown in eqs. (15) and (16) for each attitude axis $i \in \{x, y, z\}$ and specific thrust τ respectively. The gains $k_{e_1,i}, k_{e_2,i}, k_{e_3,i}$ are the diagonal elements of the gain matrices $K_{e_1}, K_{e_2}, K_{e_3}$ corresponding to axis i and k_{e_τ} is the gain for the specific thrust error. It can be seen that the error controller shapes the closed-loop response from disturbance D to attitude and specific thrust output Y, but does not affect the reference tracking dynamics.

$$Y_i = Y_{\text{ref}_i} + D_i \frac{s}{s^3 + k_{e_3,i}s^2 + k_{e_2,i}s + k_{e_1,i}} \tag{15}$$

$$Y_\tau = Y_{\text{ref}_\tau} + D_\tau \frac{s}{s + k_{e_\tau}} \tag{16}$$

Pole placement sets the desired disturbance rejection dynamics. The pseudo-actuator bandwidths are constrained by physical limits: roll and thrust by motor bandwidth ($\varepsilon_{m_l^2}, \varepsilon_{m_r^2} = 35\,\mathrm{rad\,s^{-1}}$) and pitch/yaw by elevon bandwidth ($\varepsilon_{e_l}, \varepsilon_{e_r} = 20\,\mathrm{rad\,s^{-1}}$).

The gains $k_{e_3,i} = \varepsilon_{y_i}$ set the pseudo-actuator bandwidths. The remaining gains follow from eq. (17) by expressing the closed-loop transfer function as a second-order system cascaded with an additional pole.

$$Y_i = D_i \frac{s}{(s^2 + 2\zeta_i \omega_{n_i} s + \omega_{n_i}^2)(s + p_i)} \tag{17}$$

Equating the characteristic polynomials of eq. (15) and eq. (17) yields the expression of the error controller gains in terms of the desired closed-loop dynamics parameters.

$$\begin{aligned} & s^3 + k_{e_3,i} s^2 + k_{e_2,i} s + k_{e_1,i} \\ &= (s^2 + 2\zeta_i \omega_{n_i} s + \omega_{n_i}^2)(s + p_i) \\ &= s^3 + (2\zeta_i \omega_{n_i} + p_i) s^2 + (\omega_{n_i}^2 + 2\zeta_i \omega_{n_i} p_i) s + \omega_{n_i}^2 p_i \\ &= s^3 + \underbrace{\varepsilon_{y_i}}_{k_{e_3,i}} s^2 + \underbrace{(\omega_{n_i}^2 + 2\zeta_i \omega_{n_i} \varepsilon_{y_i} - 4\zeta_i^2 \omega_{n_i}^2)}_{k_{e_2,i}} s + \underbrace{\omega_{n_i}^2 \varepsilon_{y_i} - 2\zeta_i \omega_{n_i}^3}_{k_{e_1,i}} \end{aligned} \tag{18}$$

The error controller is tuned via pseudo-actuator bandwidth ε_{y_i}, natural frequency ω_{n_i}, and damping ratio ζ_i. Table I summarizes the chosen parameters. Bandwidths match dominant physical actuators: $35\,\mathrm{rad\,s^{-1}}$ (motors) and $20\,\mathrm{rad\,s^{-1}}$ (elevons). Critical damping prevents overshoot; natural frequencies are empirically tuned through simulation and flight testing to balance disturbance rejection speed against unmodeled delays.

TABLE I: Controller Gain Design Parameters.

Parameter	**x**	**y**	**z**	$\boldsymbol{\tau}$
ε_y ($\mathrm{rad\,s^{-1}}$)	35.0	20.0	20.0	35.0
ω_n ($\mathrm{rad\,s^{-1}}$)	7.0	7.0	7.0	-
ζ (-)	1.0	1.0	1.0	-

D. Reference Model Design

The reference model shapes command tracking, while the error controller shapes disturbance rejection. Because ANDI inverts the combined aircraft and actuator dynamics, the closed-loop command-to-output dynamics equal the reference model: $\frac{Y}{U} = \frac{Y_{\text{ref}}}{U}$. Reference model design therefore directly specifies the command response.

The desired command response is parameterized by ω_{n_i}, ζ_i, and ε_{y_i}. Attitude uses a second-order model cascaded with pseudo-actuator dynamics; specific thrust uses a first-order model. The resulting transfer functions are given in eqs. (19) and (20).

$$Y_i = U_i \frac{\omega_{n_i}^2 \varepsilon_{y_i}}{(s^2 + 2\zeta_i \omega_{n_i} s + \omega_{n_i}^2)(s + \varepsilon_{y_i})} \tag{19}$$

$$Y_\tau = U_\tau \frac{\varepsilon_{y_\tau}}{s + \varepsilon_{y_\tau}} \tag{20}$$

The bandwidth parameters ε_y should not exceed the dominant physical actuator bandwidths: roll and thrust are limited by motor bandwidth ($\varepsilon_{m_l^2}, \varepsilon_{m_r^2}$), while pitch and yaw are limited by elevon bandwidth ($\varepsilon_{e_l}, \varepsilon_{e_r}$).

To realize these dynamics, a cascaded reference model generates attitude, rate, acceleration, and jerk references from the pilot command U (fig. 3). Exact quaternion kinematics with logarithmic mapping $\log(\cdot)$ handle large attitude changes without singularities [16]; a first-order model is used for specific thrust. The reference model can be augmented

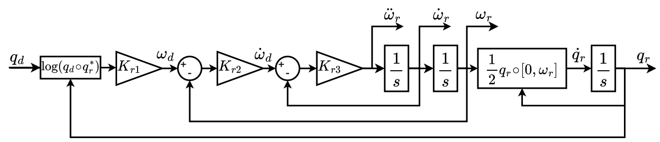

Fig. 3: Third-order attitude reference model. Converts desired attitude $\mathbf{q}_d$ into smooth references $\mathbf{q}_r, \boldsymbol{\omega}_r, \dot{\boldsymbol{\omega}}_r, \ddot{\boldsymbol{\omega}}_r$ using exact quaternion kinematics and logarithmic mapping.

by saturating the desired angular rates, accelerations, and jerk to further prevent actuator saturation. However, this saturation introduces nonlinearities into the reference model, complicating the closed-loop analysis. For simplicity, reference saturation is omitted unless explicitly specified.

The reference model structure in the Laplace domain for each attitude axis $i \in \{x, y, z\}$ and specific thrust is given in eqs. (21) and (22).

$$Y_i = Y_{\text{ref},i} = U_i \frac{k_{r_1,i} k_{r_2,i} k_{r_3,i}}{s^3 + k_{r_3,i} s^2 + k_{r_2,i} k_{r_3,i} s + k_{r_1,i} k_{r_2,i} k_{r_3,i}} \tag{21}$$

$$Y_\tau = Y_{\text{ref},\tau} = U_\tau \frac{k_{r_\tau}}{s + k_{r_\tau}} \tag{22}$$

The gains $k_{r_1,i}, k_{r_2,i}, k_{r_3,i}$ are the diagonal elements of $K_{r_1}, K_{r_2}, K_{r_3}$ and k_{r_τ} is the specific-thrust gain. They are computed by matching the reference-model characteristic polynomials to the desired dynamics.

The reference model gains are derived by equating the characteristic polynomials of eq. (21) and the desired dynamics in eqs. (19) and (20). Since all transfer functions have zero steady-state gain, only the characteristic polynomials are matched. For the specific thrust, equating the characteristic polynomials simply yields $k_{r_\tau} = \varepsilon_{y_\tau}$. For the attitude channels, the characteristic polynomial equation yields eq. (23).

$$\begin{aligned} & s^3 + k_{r_3,i} s^2 + k_{r_2,i} k_{r_3,i} s + k_{r_1,i} k_{r_2,i} k_{r_3,i} \\ &= (s^2 + 2\zeta_i \omega_{n_i} s + \omega_{n_i}^2)(s + \varepsilon_{y_i}) \\ &= s^3 + \underbrace{(2\zeta_i \omega_{n_i} + \varepsilon_{y_i})}_{k_{r_3,i}} s^2 + \underbrace{(\omega_{n_i}^2 + 2\zeta_i \omega_{n_i} \varepsilon_{y_i})}_{k_{r_2,i} k_{r_3,i}} s + \underbrace{\omega_{n_i}^2 \varepsilon_{y_i}}_{k_{r_1,i} k_{r_2,i} k_{r_3,i}} \end{aligned} \tag{23}$$

To simplify tuning and reduce the number of free parameters, the reference model parameters are typically chosen to match those of the error controller: $\omega_{n_i}, \zeta_i, \varepsilon_{y_i}$ are identical across both controllers as summarized in table I. This unified approach ensures consistent closed-loop behavior for both reference tracking and disturbance rejection.

E. Cascaded Complementary Filtering

The ANDI control law in eq. (10) relies on accurate, undelayed state estimates and feedback. Raw IMU measurements contain noise, making filtering necessary. However, filtering introduces phase lag that degrades disturbance rejection and can destabilize the closed-loop dynamics. The cascaded complementary filtering approach presented in Steffensen et al. [8] is adopted to provide undelayed estimates of angular rates, angular accelerations, body velocities, and body accelerations for feedback and compensation of state-dependent effects in the control law.

No filtering is applied to actuator-feedback signals because they exhibit sufficiently low noise. The controller computes the specific thrust τ directly from the measured motor speeds without additional filtering.

A complementary filter fuses high-frequency components from a noise-free model estimate with low-frequency components from noisy measurements.

For the On-Board Model (OBM), no additional model knowledge is required beyond what is already used in the ANDI control law. The OBM, is evaluated at the current actuator commands and state estimates to produce model-based estimates of angular acceleration $\mathbf{f}_m(\mathbf{x}, \mathbf{u}) = \dot{\boldsymbol{\omega}}_{\text{obm}}$ and body acceleration $\mathbf{f}_f(\mathbf{x}, \mathbf{u}) = \mathbf{a}_{\text{obm}}$. If no state-dependent knowledge is available, a simplified OBM that neglects state dependence can be used instead, at the cost inaccuracies in the estimated signals.

The angular acceleration and angular rate estimates come from cascaded complementary filters, expressed in the Laplace domain in eq. (24). The angular acceleration measurement $\dot{\boldsymbol{\omega}}_{\text{meas}}$ results from numerically differentiating the gyroscope measurements, while the model-based estimate $\dot{\boldsymbol{\omega}}_{\text{obm}}$ comes from evaluating the OBM at the current actuator commands and state estimates. Integrating the filtered angular acceleration $\dot{\boldsymbol{\omega}}_f$ and combining it with the gyroscope angular rate measurement $\boldsymbol{\omega}_{\text{meas}}$ yields the filtered angular rate $\boldsymbol{\omega}_f$.

$$\dot{\omega}_{f_i} = H_{\dot{\omega}_i}(s)\,\dot{\omega}_{\text{meas}_i} + (1 - H_{\dot{\omega}_i}(s))\,\dot{\omega}_{\text{obm}_i} \tag{24}$$

$$\omega_{f_i} = H_{\omega_i}(s)\,\omega_{\text{meas}_i} + \frac{1}{s}(1 - H_{\omega_i}(s))\,\dot{\omega}_{f_i} \tag{25}$$

Similarly, the controller estimates body acceleration and velocity for state-dependent dynamics compensation through complementary filtering, as shown in eq. (26). The acceleration measurement $\mathbf{a}_{\text{meas}}$ comes from the IMU accelerometer, while the model-based estimate $\mathbf{a}_{\text{obm}}$ comes from evaluating the OBM at the current actuator commands and state estimates. Integrating the filtered acceleration $\mathbf{a}_f$ and combining it with a velocity estimate $\mathbf{v}_{\text{meas}}$ yields the filtered velocity $\mathbf{v}_f$.

$$a_{f_i} = H_{a_i}(s)\,a_{\text{meas}_i} + (1 - H_{a_i}(s))\,a_{\text{obm}_i} \tag{26}$$

$$v_{f_i} = H_{v_i}(s)\,v_{\text{meas}_i} + \frac{1}{s}(1 - H_{v_i}(s))\,a_{f_i} \tag{27}$$

The undelayed state estimate $\mathbf{x}$ used in the control law eq. (10) is constructed from the filtered angular rates $\boldsymbol{\omega}_f$ and filtered body velocities $\mathbf{v}_f$. The derivative $\dot{\mathbf{x}}$ is estimated using the filtered angular accelerations $\dot{\boldsymbol{\omega}}_f$ and filtered body accelerations $\mathbf{a}_f$. These undelayed estimates are used to compute and update the control effectiveness matrix F_u and state-dependent matrix F_x in real time.

Butterworth filters attenuate high-frequency noise while minimizing phase lag. Acceleration signals use second-order filters; angular rates and velocities use first-order filters.

Table II summarizes the empirically tuned filter cutoff frequencies, which are chosen to be identical for all axes.

TABLE II: Complementary Butterworth Filter Specifications.

Filter	Purpose	Order	Cutoff Frequency
$H_{\dot{\omega}}(s)$	Angular acceleration	2nd	$\omega_{c_{\dot{\omega}}} = 20\,\mathrm{rad\,s^{-1}}$
$H_{\omega}(s)$	Angular rate	1st	$\omega_{c_{\omega}} = 80\,\mathrm{rad\,s^{-1}}$
$H_a(s)$	Translational acceleration	2nd	$\omega_{c_a} = 20\,\mathrm{rad\,s^{-1}}$
$H_v(s)$	Translational velocity	1st	$\omega_{c_v} = 80\,\mathrm{rad\,s^{-1}}$

Assuming disturbances are exogenous and independent of states and inputs, complementary filtering does not alter reference tracking dynamics but affects disturbance rejection by introducing additional poles and zeros. To characterize this effect, the closed-loop transfer function for the attitude error controller with filtering is derived by substituting the complementary filters into the closed-loop dynamics, illustrated in fig. 2. The resulting transfer function for each axis $i \in \{x, y, z\}$ is given in eq. (28).

$$\frac{Y_i}{D_i} = \frac{s^2 + (1 - H_{\dot{\omega}_i}(s))k_{e_{3,i}}s + (1 - H_{\dot{\omega}_i}(s))(1 - H_{\omega_i}(s))k_{e_{2,i}}}{s(s^3 + k_{e_{3,i}}s^2 + k_{e_{2,i}}s + k_{e_{1,i}})} \tag{28}$$

Substituting the Butterworth filter transfer functions into eq. (28) and simplifying yields the closed-loop characteristic polynomial with filtering, shown in eq. (29).

$$\underbrace{(s + \omega_{c_\omega,i})}_{H_\omega}\underbrace{(s^2 + \sqrt{2}\omega_{c_{\dot{\omega}},i}s + \omega_{c_{\dot{\omega}},i}^2)}_{H_{\dot{\omega}}}(s^3 + k_{e_{3,i}}s^2 + k_{e_{2,i}}s + k_{e_{1,i}}) \tag{29}$$

The characteristic polynomial contains the designed poles (eq. (17)) and the Butterworth filter poles. For positive cutoff frequencies ω_c, these filter poles lie in the left half-plane, so stability is preserved; however, the additional poles and zeros affect the response. This effect is minimized by using only the filtering needed for noise attenuation and is analyzed in section IV-B.

F. Controller Overview

To anchor the design, fig. 2 summarizes the attitude ANDI controller described in this section. The figure illustrates the error controller eq. (14), the incremental control law eq. (10), and the cascaded complementary filters eq. (24) that provide undelayed angular acceleration and rate estimates. Although not shown in the figure for clarity, the controller also employs translational complementary filters eq. (26) to estimate body velocities and accelerations for state-dependent dynamics compensation. The state-dependent term $F_x\dot{\mathbf{x}}$ in the incremental control law becomes significant during aggressive maneuvers with large angular accelerations, where compensation can improve tracking performance; during nominal flight with small angular rates, this compensation becomes negligible. The reference model is presented separately in fig. 3 and provides the desired state references to the controller.

The ANDI control law and all associated filters are discretized and implemented to run at $500\,\mathrm{Hz}$, yielding a Nyquist frequency of $250\,\mathrm{Hz}$. The sampling period of $2\,\mathrm{ms}$ is short relative to all relevant dynamics: the Nyquist frequency is well above both the closed-loop bandwidth (approximately $4.3\,\mathrm{Hz}$ for roll and $3.4\,\mathrm{Hz}$ for pitch and yaw) and the complementary filter cutoff frequencies (up to $80\,\mathrm{rad\,s^{-1}}$, or $12.7\,\mathrm{Hz}$). Consequently, the effects of discretization are negligible, and the continuous-time analysis and gain design presented in this section remain valid in the discrete-time implementation.

IV. Results

This section presents simulation and flight test results for the ANDI controller on the *Cyclone* tail-sitter. Simulations use `Matlab Simulink`; flight tests are indoors, limited to hover and low-speed regimes. The focus is the yaw axis, where state-dependent effects are most pronounced during aggressive heading changes.

Three experiments assess: (i) ideal tracking to verify inversion and the reference model; (ii) disturbance rejection with and without complementary filtering; (iii) the impact of state-dependent compensation versus a baseline without $F_x\dot{\mathbf{x}}$.

A. Inversion and Reference Model Verification in Simulation

Correct implementation of the control law and proper reference model design are verified by testing the closed-loop feedforward path in ideal conditions: perfect model knowledge, noiseless sensors, and no external disturbances. Under these conditions, perfect tracking of the reference trajectory confirms both the inversion and reference model dynamics.

A $170°$ heading step is applied at $t = 0.1\,\mathrm{s}$ to three configurations: full ANDI, ANDI without state-dependent compensation, and INDI baseline. ANDI uses a third-order reference model with actuator dynamics; INDI uses second-order without actuator compensation.

Dubois [13] shows that ANDI without state-dependent compensation matches INDI disturbance rejection when pseudo-actuator bandwidth equals the physical bandwidth for first-order actuators. Figure 4 validates this equivalence experimentally.

Figure 4 shows the reference trajectories and yaw attitude responses for all three controllers. The ANDI reference model exhibits slower, slightly damped dynamics compared to INDI; this reflects the explicit inclusion of actuator dynamics in the third-order reference model. The full ANDI controller with F_x tracks its third-order reference perfectly, confirming correct inversion.

ANDI without state-dependent compensation and INDI produce identical responses, validating the predicted equivalence. Both exhibit small tracking error from unmodeled state dynamics acting as a disturbance on the system. The error remains small, indicating that the state-dependent effects are minor.

Given this equivalence and the established correctness of the control law, ANDI without state-dependent compensation is used as the baseline for subsequent comparisons. This isolates the effect of $F_x\dot{\mathbf{x}}$ while keeping the remaining architecture unchanged.

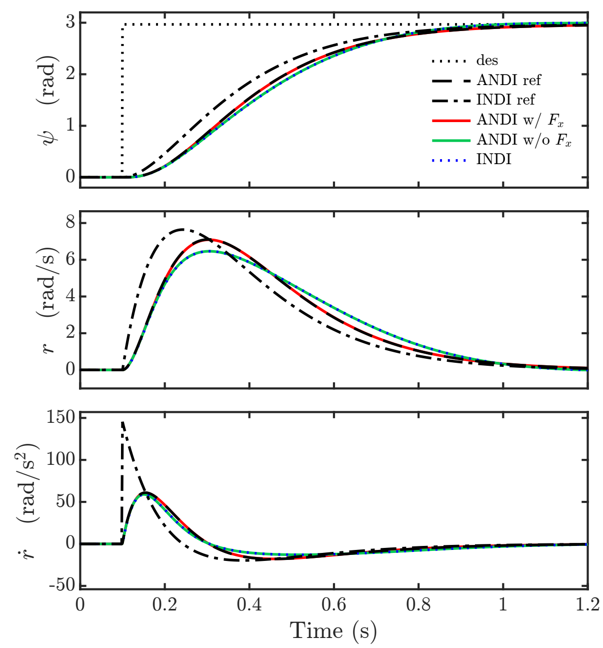

Fig. 4: Step response comparison for three controller configurations in ideal conditions, validating correct inversion and equivalence between ANDI without state effects and INDI.

B. Complementary Filtering and Disturbance Rejection in Simulation

Following verification of the control law and reference model in the feedforward path, the feedback path is examined to assess how cascaded complementary filters affect disturbance rejection. During the design of the complementary filters in section III-E, it was established that filtering should not affect closed-loop stability or reference tracking, but it can influence disturbance rejection and noise attenuation.

The full ANDI controller is tested in simulation under two conditions: with complementary filtering applied to all measurement channels, and with direct unfiltered state feedback. A step disturbance of $1.0\,\mathrm{N\,m}$ is applied to the body yaw moment at $t = 0.1\,\mathrm{s}$ in hover.

Since the disturbance is unmodeled, $F_x\dot{\mathbf{x}}$ cannot compensate for it; this analysis isolates filtering effects. With filtering, disturbances enter through the measurement path, creating a design-assumption mismatch visible in the step response.

Figure 5 shows the true heading, yaw rate, and yaw acceleration responses under filtered and unfiltered feedback. Unfiltered feedback matches the designed rejection (immediate disturbance feedback), whereas filtering slows the response and increases peak error due to low-pass lag.

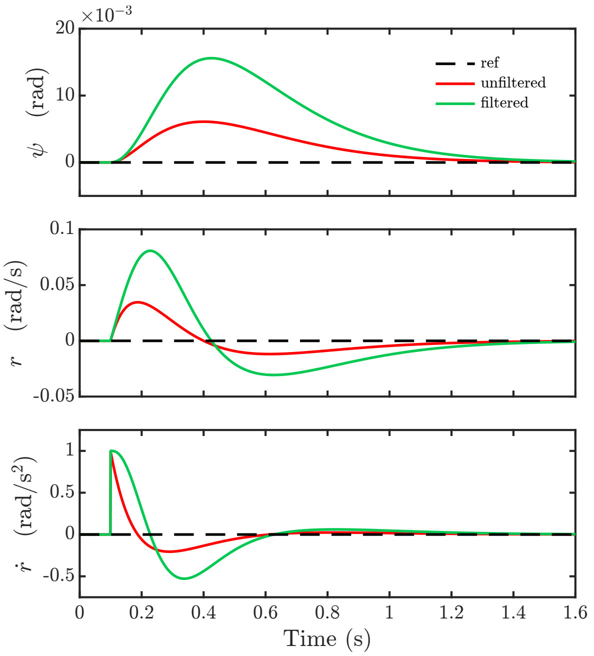

Fig. 5: Disturbance rejection comparison with and without complementary filtering. The unfiltered feedback case shows the system's designed disturbance rejection, while the filtered feedback case shows how the system's disturbance rejection degrades due to lag from low-pass filters.

The analysis demonstrates that complementary filtering, while essential for noise attenuation in real-world conditions, introduces lag that degrades disturbance rejection performance compared to ideal unfiltered feedback.

C. State-Dependent Compensation Impact in Real-World Flight Testing

Having verified the control law implementation, reference model design, and complementary filtering behavior through simulation, the final analysis assesses the practical benefits of state-dependent compensation on the physical MAV in real-world flight conditions.

A $170°$ heading step is commanded to maximize angular rates and accelerations, maximizing the influence of aerodynamic drag effects. To prevent elevon saturation, the reference model limits jerk to $100\,\mathrm{rad\,s^{-3}}$ and acceleration to $20\,\mathrm{rad\,s^{-2}}$.

Three controller configurations are tested: full ANDI (state effects in inversion and filtering), partial (state effects only in filtering), and baseline (no state effects, INDI-equivalent).

Figure 6 presents the estimated body yaw rate and acceleration responses for all three configurations, with mean responses and one standard deviation bounds from repeated flights, along with the corresponding true signals. True angular rate and acceleration are obtained via zero-phase filtering of raw IMU measurements post-flight: applying a second-order Butterworth filter ($20\,\mathrm{rad\,s^{-1}}$ cutoff) forwards and backwards through the data, eliminating phase lag and model-based assumptions.

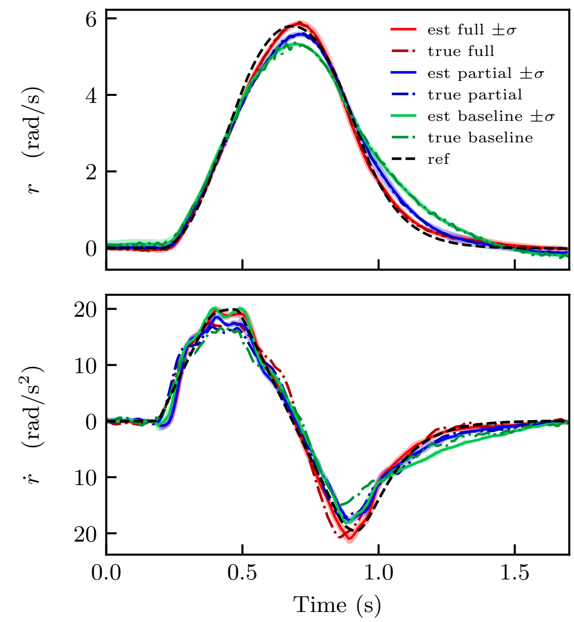

Fig. 6: Measured yaw rate and angular acceleration for a $170°$ heading step applied at $0.2\,\mathrm{s}$ during flight testing. Plotted are the three controller configurations: full ANDI (state effects in inversion and complementary filtering), partial ANDI (state effects only in complementary filtering), and baseline (no state effects, INDI-equivalent). True acceleration is obtained through zero-phase low-pass filtering of the raw IMU measurements.

From the estimated signals in fig. 6, all three controllers achieve stable flight and excellent tracking of the commanded heading step for both angular rate and acceleration. The reference model effectively shapes the closed-loop dynamics, with all configurations exhibiting similar overall response characteristics.

Complementary filtering effectively attenuates noise and provides clean estimates consistent with table II. Transient mismatches between estimated and true acceleration are attributed to unmodeled higher-order effects.

Performance differences are most evident at high angular rates and accelerations where aerodynamic drag becomes significant. The full ANDI achieves best tracking with close estimated-to-true acceleration agreement, while partial shows intermediate performance and baseline performs worst.

Table III summarizes Root Mean Square (RMS) tracking errors for estimated (used by the error controller) and true (actual MAV performance) yaw rate and acceleration.

The RMS results confirm state-dependent compensation benefits. Rate RMS is more representative of controller performance since it follows from the acceleration tracking.

TABLE III: RMS Tracking Errors

RMS error	Full	Partial	Baseline
r_{est} (rad s^{-1})	0.146	0.243	0.430
$\dot{r}_{\text{est}}$ (rad s^{-2})	1.278	1.676	2.332
r_{true} (rad s^{-1})	0.151	0.246	0.450
$\dot{r}_{\text{true}}$ (rad s^{-2})	2.092	2.071	2.707

Estimated yaw rate error reduced $66\,\%$ for full ANDI and $43\,\%$ for partial versus baseline, with estimated yaw acceleration showing $45\,\%$ and $28\,\%$ reductions respectively. While true acceleration RMS errors for full and partial are nearly identical (2.092 and 2.071 rad s^{-2}), both substantially outperform the baseline (2.707 rad s^{-2}). Notably, fig. 6 reveals qualitative differences: full ANDI slightly overshoots the true acceleration signal instead of undershooting it like in the partial case, resulting in the observed improvement in rate tracking.

D. Discussion

The experimental validation confirms ANDI implementation correctness and practical viability. Control law inversion is verified through perfect reference tracking in simulation; ANDI–INDI equivalence is experimentally demonstrated; cascaded complementary filtering is validated in real-world flight. State-dependent compensation yields measurable improvements during aggressive maneuvers, particularly on platforms with pronounced aerodynamic drag. However, practical relevance depends on platform characteristics: for MAVs with negligible state-dependent effects or benign operating regimes, baseline ANDI without F_x suffices. ANDI unifies classical INDI while offering flexible incorporation of actuator dynamics and state-dependent compensation when needed.

V. Conclusion

This work implements and validates ANDI with explicit state-dependent compensation on the *Cyclone* tailsitter MAV. ANDI is demonstrated as a practical attitude stabilization framework that generalizes classical INDI by incorporating actuator dynamics and state-dependent effects.

State-dependent compensation yields clear benefits during aggressive maneuvers (66% yaw-rate error reduction). ANDI is the preferred framework due to its generality: it reduces to INDI without additional modeling effort while retaining capability for state-dependent effects when justified.

All tests were conducted indoors in hover and low-speed flight on a single platform. The observed benefits are conservative and may underestimate impact in high-speed or aggressive transition maneuvers.

Future work should extend ANDI to guidance control with state-dependent body-force compensation, repeat experiments across wider operational envelopes (outdoor high-speed flight, transition maneuvers), and validate on additional platforms.

References

[1] A. S. Saeed, A. B. Younes, C. Cai, and G. Cai, “A Survey of Hybrid Unmanned Aerial Vehicles,” *Progress in Aerospace Sciences*, Mar. 1, 2018. DOI: 10.1016/j.paerosci.2018.03.007.

[2] H. K. Khalil, “Nonlinear Systems,” in 3rd ed. Prentice Hall, 2002, ch. 6, pp. 207–275.

[3] D. Surmann, M. Zrenner, and S. Myschik, “Flight Performance Evaluation of a Conceptual Evtol System Using Nonlinear Simulations,” in *AIAA SCITECH 2022 Forum*, Jan. 3, 2022. DOI: 10.2514/6.2022-2220.

[4] A. Steinleitner, V. Frenzel, O. Pfeifle, J. Denzel, and W. Fichter, “Automatic Take-Off and Landing of Tailwheel Aircraft with Incremental Nonlinear Dynamic Inversion,” in *AIAA SCITECH 2022 Forum*, Dec. 29, 2021. DOI: 10.2514/6.2022-1228.

[5] E. J. J. Smeur, Q. Chu, and G. C. H. E. de Croon, “Adaptive Incremental Nonlinear Dynamic Inversion for Attitude Control of Micro Air Vehicles,” *Journal of Guidance, Control, and Dynamics*, vol. 39, no. 3, pp. 450–461, Mar. 2016. DOI: 10.2514/1.G001490.

[6] R. Steffensen, A. Steinert, and E. J. J. Smeur, “Nonlinear Dynamic Inversion with Actuator Dynamics: An Incremental Control Perspective,” *Journal of Guidance, Control, and Dynamics*, pp. 1–9, Nov. 25, 2022. DOI: 10.2514/1.G007079.

[7] T. M. L. De Ponti, E. J. J. Smeur, and B. D. W. Remes, “Unified-Actuator Nonlinear Dynamic Inversion Controller for the Variable Skew Quad Plane,” *Journal of Guidance, Control, and Dynamics*, pp. 1–10, Feb. 13, 2025. DOI: 10.2514/1.G008659.

[8] R. Steffensen, A. Steinert, Z. Mbikayi, S. Raab, J. Angelov, and F. Holzapfel, “Filter and sensor delay synchronization in incremental flight control laws,” *Aerospace Systems*, vol. 6, no. 2, pp. 285–304, Jun. 1, 2023. DOI: 10.1007/s42401-022-00186-2.

[9] M. Bronz, E. J. Smeur, H. G. de Marina, and G. Hattenberger, “Development of A Fixed-Wing mini UAV with Transitioning Flight Capability,” in *35th AIAA Applied Aerodynamics Conference*, Jul. 2, 2017. DOI: 10.2514/6.2017-3739.

[10] G. Hattenberger, M. Bronz, and M. Gorraz, “Using the Paparazzi UAV System for Scientific Research,” in *International Micro Air Vehicle Conference and Competition 2014*, Aug. 12, 2014, pp 247. DOI: 10.4233/uuid:b38fbdb7-e6bd-440d-93be-f7dd1457be60.

[11] L. R. Lustosa, F. Defaÿ, and J.-M. Moschetta, “Global Singularity-Free Aerodynamic Model for Algorithmic Flight Control of Tail Sitters,” *Journal of Guidance, Control, and Dynamics*, vol. 42, no. 2, pp. 303–316, Feb. 2019. DOI: 10.2514/1.G003374.

[12] E. A. Tal and S. Karaman, “Global Incremental Flight Control for Agile Maneuvering of a Tailsitter Flying Wing,” *Journal of Guidance, Control, and Dynamics*, vol. 45, no. 12, pp. 2332–2349, Dec. 12, 2022. DOI: 10.2514/1.G006645.

[13] J. P. G. Dubois, “Full Actuator Nonlinear Dynamic Inversion for Enhanced Hybrid UAV Control,” Delft, Feb. 11, 2026. https://repository.tudelft.nl/record/uuid:5640fa42-1c33-4639-838f-5fda5b4cb37f Accessed: Feb. 13, 2026.

[14] E. J. J. Smeur, M. Bronz, and G. C. H. E. de Croon, “Incremental Control and Guidance of Hybrid Aircraft Applied to a Tailsitter Unmanned Air Vehicle,” *Journal of Guidance, Control, and Dynamics*, vol. 43, no. 2, pp. 274–287, Sep. 17, 2020. DOI: 10.2514/1.G004520.

[15] R. Van ’t Veld, “Incremental Nonlinear Dynamic Inversion Flight Control,” Master of Science Thesis, Delft University of Technology, Delft, Sep. 29, 2016. https://repository.tudelft.nl/file/File_72437d3f-ba51-4718-be28-a368de7d02f3 Accessed: Mar. 25, 2025.

[16] J. Solà, “Quaternion Kinematics for the Error-State Kalman Filter,” Nov. 3, 2017. DOI: 10.48550/arXiv.1711.02508.